

Designer Heavy Fermions in Incommensurate Nb₃Cl₈/Graphene van der Waals Heterostructures

Yuchen Gao¹, Wenjie Zhou¹, Fan Yang¹, Zhijie Ma^{2,3}, Hansheng Xu¹, Xinyue Huang^{1,4},
Kenji Watanabe⁵, Takashi Taniguchi⁶, Youguo Shi^{2,3,*}, Yu Ye^{1,7,8,9,*}

¹ State Key Laboratory for Artificial Microstructure & Mesoscopic Physics and Frontiers Science Center for Nano-Optoelectronics, School of Physics, Peking University, Beijing 100871, China

² University of Chinese Academy of Sciences, Beijing 100049, China

³ Songshan Lake Materials Laboratory, Dongguan, Guangdong 523808, China

⁴ Academy for Advanced Interdisciplinary Studies, Peking University, Beijing 100871, China

⁵ Research Center for Electronic and Optical Materials National Institute for Materials Science 1-1 Namiki, Tsukuba 305-0044, Japan

⁶ Research Center for Materials Nanoarchitectonics National Institute for Materials Science 1-1 Namiki, Tsukuba 304-0044, Japan

⁷ Collaboration International Center of Quantum Matter, Beijing 100871, China

⁸ Liaoning Academy of Materials, Shenyang 110167, China

⁹ Yangtze Delta Institute of Optoelectronics, Peking University, Nantong 226010, Jiangsu, China

* Email: ygshi@iphy.ac.cn, ye_yu@pku.edu.cn

Abstract

Heavy fermion systems, traditionally realized in rare-earth compounds with limited tunability, have hindered systematic exploration of correlated quantum phenomena. Here, we introduce a general strategy for engineering heavy fermions in incommensurate van der Waals heterostructures by coupling a Mott insulator (Nb₃Cl₈) with itinerant electrons (from monolayer graphene), circumventing strict lattice-matching requirements. Through magnetotransport and slave spin mean-field calculations, we demonstrate the hybridization gap ($\Delta \approx 30$ meV), gate-tunable metal-insulator transition, and band-selective electron effective mass enhancement, hallmarks of Kondo coherence. The heterostructure exhibits nearly order-of-magnitude electron effective mass dichotomy between hybridized and conventional graphene-like regimes, alongside in-plane magnetic field-induced metal-insulator transitions. Top gate-temperature phase mapping reveals competing correlated states, including insulating and hidden-order phases. This work establishes a scalable platform for designing heavy fermion by replacing the itinerant electron materials, with implications for engineering topological superconductivity and quantum criticality in low-dimensional systems.

Introduction

Heavy fermion systems exemplify strongly correlated quantum matter, hosting rich phenomena such as quantum criticality, non-Fermi liquid behavior¹, topology², and unconventional superconductivity^{3,4}. The effective mass of electrons in such systems undergoes a substantial renormalization via itinerant-localized hybridization, a phenomenon that can be modeled using the periodic Anderson model. Despite decades of intensive research, traditional realizations in bulk rare-earth compounds suffer from limited tunability and structural complexity, hindering systematic exploration of correlated phases^{5,6}. Recent breakthroughs in van der Waals (vdW) heterostructures have introduced designer platforms for heavy fermions, including moiré-engineered MoTe₂/WSe₂⁷ and commensurate 1T/1H TaS₂ heterolayers⁸. vdW heterostructures enable *in situ* control of Kondo lattice interactions and quantum criticality. However, commensurate structures are constrained by layer-to-layer lattice matching requirements and are restricted by system-limited itinerant electrons. The field urgently requires adaptable platforms that decouple itinerant and localized degrees of freedom, permitting arbitrary component substitution while retaining gate-tunable correlations. Achieving such versatility in vdW heterostructures would establish a universal phase space to probe intertwined, strongly correlated orders, thereby revolutionizing our understanding of quantum matter.

We explicitly demonstrate the emergence of heavy fermion within a distinctive configuration in which a layer of itinerant electrons is stacked upon another flat-band Mott insulator layer. In this unique set-up, the nearly half-filled flat band accommodates localized electrons, while the interlayer hopping facilitates the hybridization of itinerant and localized electron orbits, as elucidated in Fig. 1a. For our experimental framework, Nb₃Cl₈ serves as the Mott insulator, distinguished by a prominent half-filled flat band with a bandwidth of approximately 200 meV and Hubbard U of 1.2 eV⁹. The localized electrons within the half-filled flat band are predominantly located in the center of the Nb₃ clusters¹⁰. Monolayer graphene (MLG) introduces dispersive bands into the system. Density functional theory (DFT) calculations reveal a near-ideal band alignment (Fig. 1b), with graphene’s slight p -doping preserving the flat band’s half-filling. Crucially, interfacial hybridization leads to the opening of a hybridization gap on the order of several tens of meV (inset of Fig. 1b), a hallmark of coherent Kondo screening despite DFT’s inherent limitations in modeling strong correlations. This vdW heterostructure effectively embodies the essential ingredients of the periodic Anderson model: localized moments coupled with metallic states through spatially resolved orbital overlap.

In investigating the tunability of the heavy fermions, we fabricated dual-gated heterostructure devices (Fig. 1c and Fig. 1d), without intentional twist control, given the inherent lattice mismatch between Nb₃Cl₈ (6.833 Å) and MLG (2.468 Å)¹¹. The observed phenomena exhibit consistency across all five devices, with another representative case illustrated in Extended Data Figure S1. The design incorporating dual gates allows for independent manipulation of carrier density and electric field within the sample. However, while top-gate sweeps at 2 K revealed negligible hysteresis, back-gate sweeps mediated by Nb₃Cl₈ exhibited distinct bistability between high- and low-resistance states. The device naturally transitions to a high-resistance state upon cooling from room temperature to 2 K, whereas achieving the low-resistance state necessitates sweeping the back-gate voltage (V_{BG}) at 2 K, with a relaxation time exceeding 10 hours (Extended Data Figure S2). The universality of this hysteresis phenomenon, evident across all devices, hints at the

emergence of ferroelectricity (a topic to be separately addressed), hindering the practical utilization of the back gate. This study concentrates on the top-gate-tunable high-resistance regime at a fixed $V_{BG}=0$ V to delineate correlation effects.

Figure 1e reveals gate-tunable correlation effects through temperature-dependent resistance at a top-gate voltage (V_{TG}) of -1 V and 4 V in the absence of a magnetic field. Below 10 K, the resistance at $V_{TG} = -1$ V remains nearly constant with temperature, while the resistance at $V_{TG} = 4$ V exhibits a sharp rise — both obeying $R = R_0 + AT^2$ Fermi liquid scaling¹², where R_0 denotes residual resistance stemming from impurity scattering and $A^{0.5}$ is directly proportional to the effective mass of the Fermi liquid. Crucially, the $V_{TG} = 4$ V data yield nearly an order of magnitude larger $A^{0.5}$ value *versus* $V_{TG} = -1$ V, signaling an enhancement in the quasiparticle mass of the top gate configuration of 4 V compared to the counterpart of -1 V. Paradoxically, the 2 K resistance value at $V_{TG} = 4$ V doubles that at $V_{TG} = -1$ V, implying lower carrier density despite conventional MLG physics predicting larger electron effective masses at higher carrier density. This contradiction exposes a marked departure from MLG’s intrinsic behavior, a direct signature of interfacial quantum reconstruction induced by Nb₃Cl₈.

Band structure and the emergent flat band

To unravel this discrepancy and delve into interfacial band reconstruction, we conducted magneto-transport measurements that unveiled gate-tunable quantum oscillations. Figure 2a charts the symmetrized longitudinal resistance (R_{xx}) across V_{TG} and perpendicular magnetic field, delineating two distinct regimes demarcated by red dashed lines. Within the domain of the small V_{TG} (<0 V, regime II), the Landau fan diagram’s construction reveals linear profiles akin to conventional MLG behavior. Conversely, in the large top gate region (regime I), the Landau levels exhibit a steeper trajectory with discernible minor kinks. The low-field Hall-derived carrier density corroborates this transition (Extended Data Figure S3). The pronounced increase in the Landau levels’ slope upon transitioning across the boundary signifies a distinct charge transfer, where crossing into regime I activate charge transfer into states beyond graphene’s Dirac cone^{13,14}. The field-tilted phase boundary (red dashed lines in Fig. 2a) underscores the field-responsive nature of band alignment. Crucially, the hybrid states’ high density of states (DOS) enforces persistent p -doping, effectively locking the system away from charge neutrality — a stark departure from MLG’s gate-response paradigm.

This charge transfer phenomenon is indicative of the evolution of the DFT band structure, wherein the Fermi level (E_F) initially rises from below the flat band (pure graphene-dominated transport) and eventually reaches and stabilizes at the flat band. However, the model predicts a complete depletion of Nb₃Cl₈’s half-filled flat band in regime II, resulting in hole-doping with a carrier density ($\sim 10^{14}$ cm⁻²) that far exceeds both top gate-induced and Shubnikov-de Haas (SdH) oscillation-derived densities ($\sim 10^{12}$ cm⁻², see Extended Data Figure S4). This paradox can be resolved through the concept of orbital-selective Mott correlations¹⁵, which involves incorporating Nb₃Cl₈’s large and screening-insensitive Hubbard U (~ 1.2 eV)¹⁰, along with interlayer hybridization. Initially, isolated components exhibit MLG’s Dirac cone and Nb₃Cl₈’s flat band (Fig. 2b, upper panel). Introducing interlayer hybridization alone produces the DFT calculated band structure (Fig. 2b, middle left panel), while only activating on-site Hubbard U produces split Hubbard bands coexisting with MLG’s Dirac cone (Fig. 2b, middle right panel). It is imperative to acknowledge that the concurrent hybridization and Hubbard U redistribute quasiparticle spec-

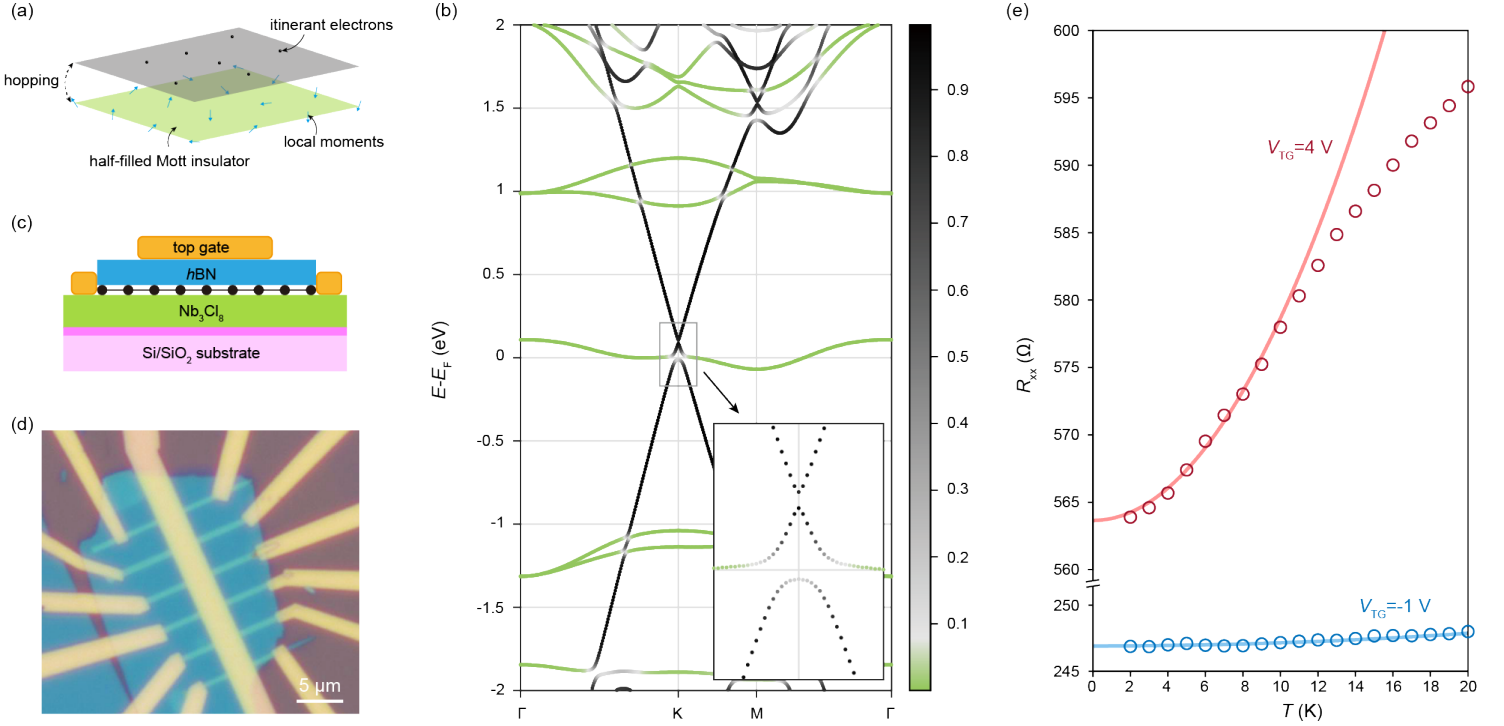


Fig. 1 Structural and electronic properties of the Nb₃Cl₈/MLG heterostructure. **a**, Schematic of the heterostructure. Monolayer graphene (MLG, gray) hosts itinerant carriers, while Nb₃Cl₈ (green) layer forms a Mott insulator with localized moments at Nb₃ clusters. Interlayer electron hopping realizes the periodic Anderson model. **b**, DFT-calculated band structure of Nb₃Cl₈/MLG heterostructure. The Dirac cone of the MLG hybridizes with Nb₃Cl₈'s half-filled flat band, opening a hybridization gap in the vicinity of the K point. Inset: the zoomed DFT band structure near the Fermi level. The color bar denotes the carbon orbital weight. **c-d**, Side view (c) and optical image (d) of the dual-gated Hall bar device. **e**, Temperature-dependent resistance at $V_{TG} = -1$ V and $V_{TG} = 4$ V. Both curves follow $R = R_0 + AT^2$ (solid lines), confirming Fermi liquid nature. The contrasting residual resistance R_0 and coefficient A highlight distinct electronic states.

tral weight, coalescing the original two Hubbard bands into three reconstructed bands of lower incoherent, middle hybrid, and upper incoherent bands (Fig. 2b, bottom) near the K point. The coherence of the hybridized middle band (with the itinerant bands) drives the interfacial many-body reconstruction, manifesting as either a heavy fermion metal^{16,17} or a Kondo insulator¹⁸ contingent on E_F 's position relative to the hybridization gap.

This low-energy band configuration (Fig. 2b, pink dashed box) aligns with DFT outcomes but exhibits finite quasiparticle weight in the middle coherent band at E_F . Notably, the lower band retains graphene-like dispersion due to MLG's high Fermi velocity, which is consistent with conventional MLG transport behavior observed in regime II. Increasing V_{TG} drives the Fermi level from the lower band to the middle band, marking coherent charge transfer into hybridized states. The band-resolved analysis quantitatively explains both the observed interfacial charge transfer and MLG's low carrier density, establishing gate-controlled hybridization as the mechanism underpinning correlated electron physics in the heterostructure.

The band reconstruction scenario predicts a hybridization gap near the phase boundary, a key signature of heavy fermion formation. Experimentally, an anomalous insulator-like R - T curve emerges at $V_{TG} = 0$ V (Fig. 2c), exhibiting negative dR/dT above 5 K, distinct from metallic responses at other gate voltages either above or below the phase boundary (Fig. 1e). The insulator-like behavior indicates a gap at the phase boundary. Temperature-dependent Hall measurements reveal thermally activated carriers across this gap (Fig. 2d), with density evolution well-described by $n = n_0 + n_1/(1+\exp(\Delta/kT))$, where n_0 represents residual carrier density stemming from in-gap states and impurity bands, n_1 de-

notes the effective DOS at the band edge, and Δ signifies the excitation gap. The fitted $\Delta \approx 28.7$ meV confirms strong graphene-flat band hybridization. Two sharp resistance peaks in the R - V_{TG} profile at 2 K under zero magnetic field (Fig. 2e) demarcate insulating regimes: one near charge transfer ($V_{TG} = 0.3$ V) and another signaling middle-band complexity ($V_{TG} = 3$ V). The discrepancy in V_{TG} between the insulating R - T curve ($V_{TG} = 0$ V) and the peak resistance R - V_{TG} curve ($V_{TG} = 0.3$ V) may be attributable to residual carriers. The extracted residual carrier density is substantially large ($n_0 \approx 7.5 \times 10^{11} \text{ cm}^{-2}$), dominating low-temperature transport at the charge transfer boundary via in-gap states, causing marked instability in the R - T curve at 0 V top gate below 50 K (Extended Data Figure S5), which is influenced by historical factors and electric noise on the top gate. Notably, the manifestation of in-gap states echoes phenomena observed in Kondo insulators^{19,20}. Despite the high quality demonstrated by SdH oscillations, dismissing impurity effects, the presence of in-gap states may stem from misalignments of the hybridization gap across disparate or inhomogeneous real-space regions, induced intrinsically by incommensurate MLG/Nb₃Cl₈ lattices or extrinsically by the dry transfer process. Crucially, gate-stable gap signatures persist despite disorder effects, establishing interfacial quantum reconstruction as the governing paradigm.

The experimental evidence of charge transfer and interfacial hybridization gap unambiguously validates the proposed band reconstruction and establishes the heterostructure as a heavy fermion system. This places the system in a mixed-valence regime²¹, where the filling of Nb₃Cl₈'s localized flat band is continuously tuned by the top gate. The observed gate-tunable effective electron mass dichotomy stems from contrasting flat band contributions: The middle band's dominant flat band character under positive V_{TG}

drives electron effective mass renormalization, while the lower band's graphene-like dispersion at negative V_{TG} yields conventional behavior. This spectral weight asymmetry directly links band dispersion to emergent quantum phases.

Slave spin mean-field calculation and microscopic mechanism

To elucidate the microscopic picture of the observed heavy fermion behavior, including the emergent coherent flat band, charge transfer behavior, and distinct electronic regimes across the charge transfer phase boundary, we employ a slave spin mean-field (SSMF) calculation tailored to the $\text{Nb}_3\text{Cl}_8/\text{MLG}$ heterostructure (Fig. 3a and see details in Supplementary Note I). This approach, grounded in the periodic Anderson model, captures key mechanisms of heavy fermion systems by decoupling localized electrons into separate spin and fermionic operators under a mean-field constraint (see details of SSMF calculation in Supplementary Note II). While standard DFT fails to describe correlation-driven phenomena, the SSMF framework renormalizes hybridization, bandwidth, and onsite energies, enabling direct comparison with experimental trends.

As the bare hybridization strength increases, the SSMF calculation unveils a phase transition from an orbital-selective Mott phase to a heavy fermion phase, characterized by the emergence of a quasiparticle weight (Fig. 3b). In the heavy fermion regime, the theory predicts a coherent flat band that hybridizes with the dispersive bands of MLG, opening a gap at the K point, in alignment with our experimental findings (the position determined by the gap size is marked by the red star in the phase diagram). The system's position in the heavy fermion is further corroborated by the enhanced electron effective mass of the middle band (Supplementary Note III and Fig. S2), aligning with transport data. Notably, the observed gap size requires a larger hybridization coefficient than predicted by DFT, a discrepancy attributed to the PBE functional's known underestimation of electronic gap²². While SSMF successfully reproduces the flat band's emergence, gap formation, and electron effective mass renormalization, it systematically underestimates bandwidth due to neglected quantum fluctuations. For instance, the model predicts a zero-bandwidth Mott state, whereas angle-resolved photoemission spectroscopy (ARPES) reveals a finite bandwidth of Hubbard bands in Nb_3Cl_8 ⁹. Despite these limitations, the theory offers a qualitatively sound conceptual framework by manually addressing these discrepancies.

Initially, according to the mean-field constraint condition, the E_F consistently intersects the emergent coherent band. However, the quasiparticle weight of the coherent band nears zero due to Nb_3Cl_8 's substantial Hubbard U , triggering robust onsite energy renormalization of the coherent band. This ultimately leads to the coherent band tracking the E_F instead of pinning it. The renormalized onsite energy of the coherent band facilitates efficient gate-tuning of MLG's carrier density, a pivotal feature absent in DFT. Furthermore, a pronounced DOS peak near the half-filling of the Nb_3Cl_8 band (Fig. 3c) governs charge transfer, akin to non-interacting systems. All these facets elucidates the scenario near the charge transfer boundary (Fig. 3d). Originating from the lower band phase, with the increasing of V_{TG} , the E_F ascends, consequently elevating the flat band due to onsite energy renormalization, enabling carriers to populate the MLG bands. As $V_{TG} \approx 0$ V, the system transitions into the Kondo insulator phase, where the E_F resides within the gap, engendering insulating behavior in the heterostructure. The E_F also touches the ultra-flat band, contributing to the DOS peak near zero top gate, ushering the system into regime I. Subsequently, as E_F continues its ascent, the system traverses

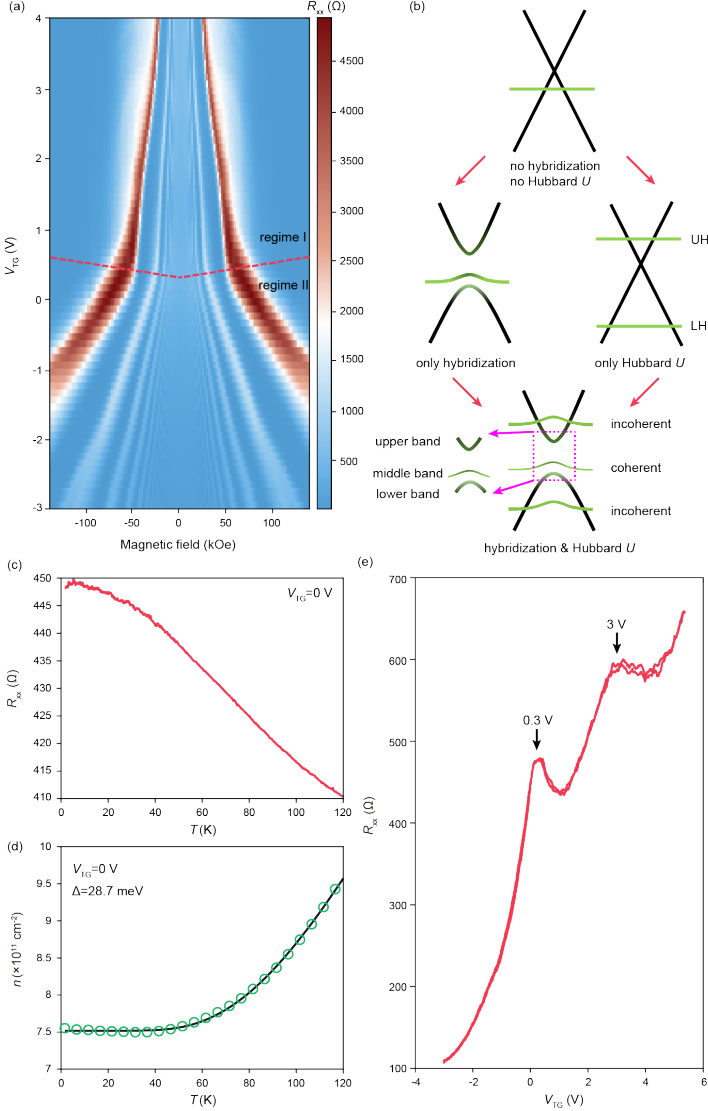


Fig. 2 Electronic band structure and transport properties of the $\text{Nb}_3\text{Cl}_8/\text{MLG}$ heterostructure. **a**, Resistance versus V_{TG} and magnetic field at 2 K. The red dash lines demarcate two regimes. In regime I, the electrons populate in both MLG and additional electron states, resulting in a steeper shape of the Landau fan diagram. In regime II, electrons adjacent to the K point fill in the MLG-like band, and the Landau fan diagram is analogous to that of a conventional MLG. **b**, Schematic band structure evolution with interlayer hybridization and Hubbard U . The color of the lines represents the layer component of the wave function. More specifically, the MLG orbit and the Nb_3Cl_8 orbit are denoted as black and green, respectively. The upper panel shows the band structure without hybridization and Hubbard U . The middle left and the middle right panels show the band structure only with hybridization and Hubbard U , respectively. The lower panel shows the band structure with both hybridization and Hubbard U , where the original two Hubbard bands in the middle right panel split into two incoherent bands and one coherent band that hybridizes with MLG bands, forming a low-energy three-band structure shown in the inset. **c**, Temperature-dependent resistance at $V_{TG} = 0$ V. Insulating behavior confirms a hybridization gap. **d**, Temperature-dependent carrier density (green circles) at $V_{TG} = 0$ V extracted from temperature-dependent Hall measurements. The Fermi-Driac distribution fit (black line) extracts a 28.7 meV band gap. **e**, V_{TG} -dependence resistance at 2 K and without a magnetic field. Peaks at $V_{TG} = 0.3$ V and $V_{TG} = 3$ V (arrows) mark phase boundaries.

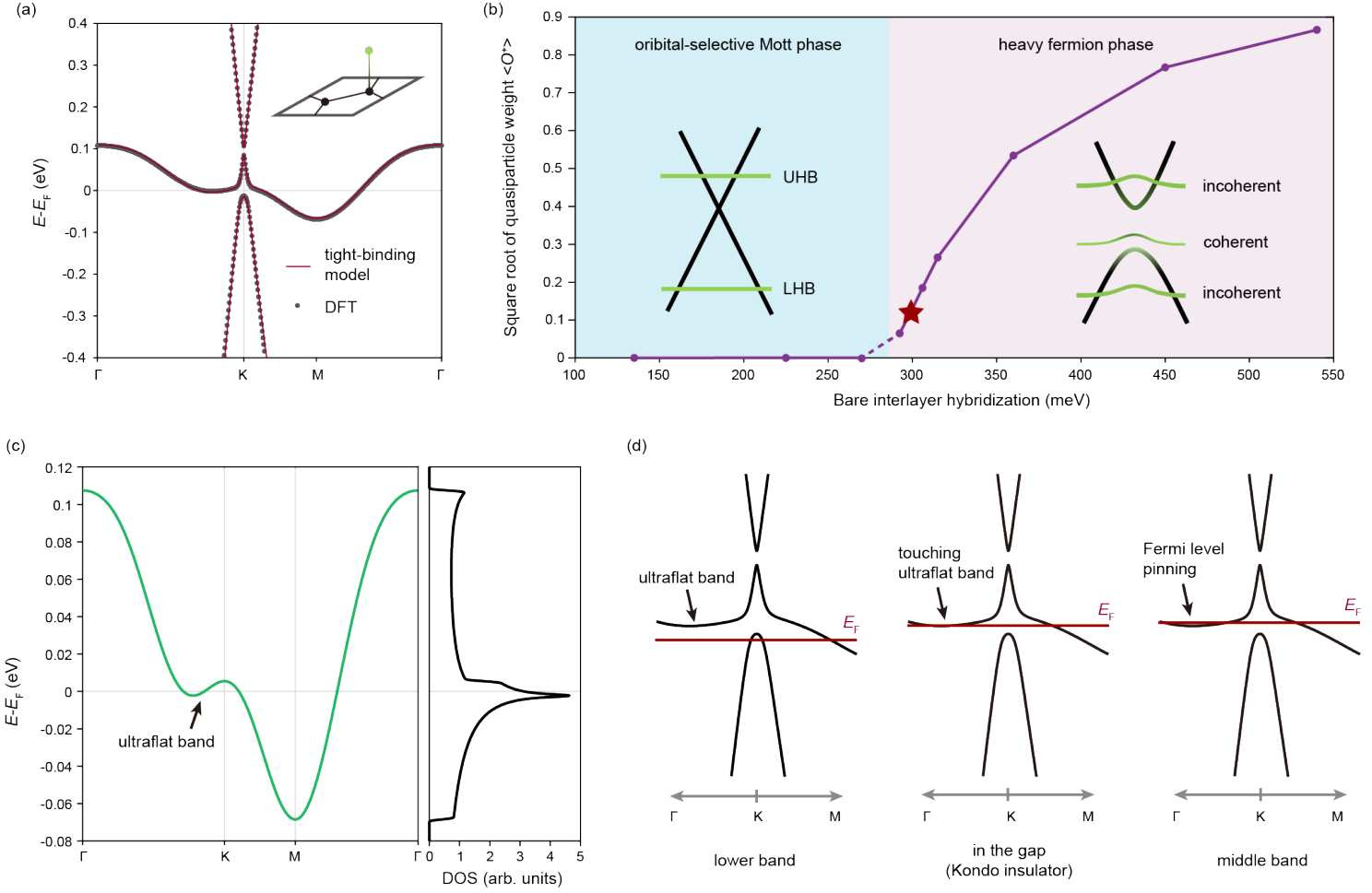


Fig. 3 Microscopic mechanism of correlated phenomena in the $\text{Nb}_3\text{Cl}_8/\text{MLG}$ heterostructure. **a**, DFT-calculated (gray dots) and tight-binding model calculated (red lines) of the low-energy band structure of the heterostructure. The strong agreement confirms the tight-binding model's validity for low-energy physics. Inset: Schematic of the tight-binding model geometry (black dots: MLG carbon atoms; green dot: Nb_3 cluster). **b**, Phase diagram from SSMF calculations. The order parameter $\langle O^+ \rangle$ (square root of quasiparticle weight) transitions abruptly from zero to a finite value at a critical bare hybridization coefficient, signaling the emergence of the coherent band and the phase transition from the orbital-selective Mott phase to the heavy fermion phase. The star denotes the system's experimental position, determined by matching the observed hybridization gap. **c**, Tight-binding band structure (left panel) and DOS (right panel) for isolated Nb_3Cl_8 . An ultra-flat band near the K point generates a near zero-energy DOS peak. **d**, Band structure and Fermi level evolution near the charge transfer phase boundary. Left: E_F in the lower band (metallic regime, regime II). Middle: E_F enters the hybridization gap at the K point (Kondo insulator phase). E_F also touches the ultra-flat band in the gap, producing the charge transfer behavior. Right: E_F crosses the middle band (regime I), where electron effective mass renormalization enhances correlations.

into another metallic phase, accompanied by an enhancement in electron effective mass. It is crucial to note that the three-band depiction (comprising the upper, middle, and lower bands) is distinctly defined in the vicinity of the K point, while the E_F in all three phases is delineated in Fig. 3d. Significantly, the three-band representation near the K point, where MLG governs transport by its superior mobility, rationalizes the observed metal-insulator transition and anomalous temperature-dependent behavior. By bridging correlations, band properties, and gate response, the SSMF framework establishes $\text{Nb}_3\text{Cl}_8/\text{MLG}$ as an exemplary heavy fermion heterostructure embodying intertwined quantum phases.

V_{TG} versus T phase diagram

Our comprehensive phase mapping uncovers rich correlation-driven phenomena in the $\text{Nb}_3\text{Cl}_8/\text{graphene}$ heterostructure. Figure 4a displays the temperature-dependent resistance measured at varied V_{TG} . The low-temperature data aligns with our theoretical model, exhibiting two distinct regimes: (i) At negative V_{TG} , the E_F intersects the lower band's graphene-like dispersion, yielding in

marginal resistance variation from 2-20 K — a hallmark of weak correlations. (ii) Positive V_{TG} shifts E_F into the hybridized middle band, driving pronounced resistance increases with temperature (e.g., $+10.6 \, \Omega$ at $V_{\text{TG}}=2 \, \text{V}$, 2-20 K). Near the charge transfer boundary ($V_{\text{TG}} \approx 0 \, \text{V}$), anomalous insulating behavior emerges (negative dR/dT above 5 K), signaling a Kondo insulator scenario in our microscopic model. The derived dR/dT map across the $V_{\text{TG}}-T$ parameter space (Fig. 4b) reveals critical phase boundaries underpinning the system's quantum complexity. The charge transfer boundary demarcates a prominent insulating zone, corresponding to the hybridization gap discussed earlier, which dominates transport. At elevated temperatures, the insulating region extends into regime I at higher V_{TG} (green dashed line, Fig. 4b), a signature of heavy fermion metals characterized by low carrier densities^{23,24}. Centered at 40 K and $V_{\text{TG}} = 3 \, \text{V}$, a high-temperature insulator-like phase emerges, coinciding with the resistance peak in Fig. 2e, and may originate from another kind of incoherent Kondo scattering. In regime II at V_{TG} from $-2 \, \text{V}$ to $0 \, \text{V}$, we observe a rapid resistance increase near 40 K. At strongly negative V_{TG} ($-3 \, \text{V}$ to $-2 \, \text{V}$), a low-temperature

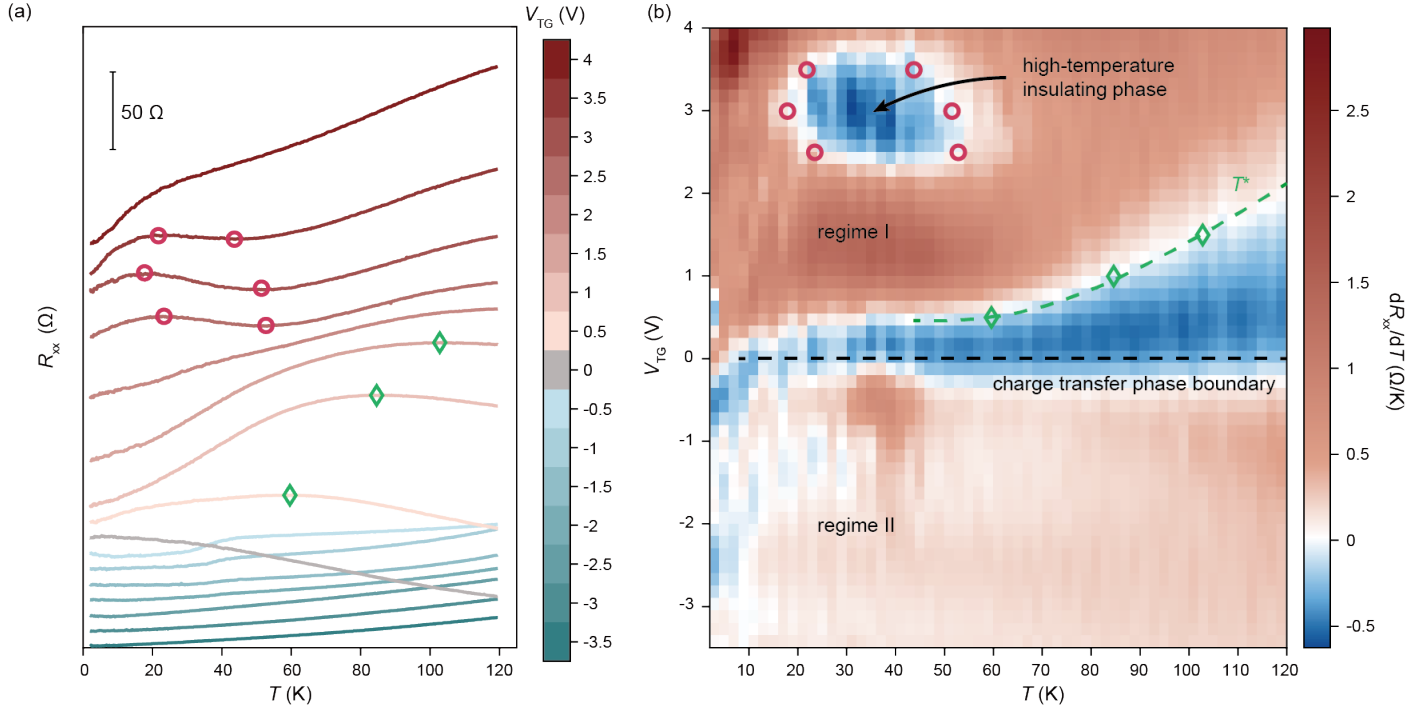


Fig. 4 Gate-temperature-tunable phase diagram of the $\text{Nb}_3\text{Cl}_8/\text{MLG}$ heterostructure. **a**, The shifted temperature-dependent resistance at various V_{TG} from -3.5 V to 4 V. AT $V_{\text{TG}} = 0$ V (gray curve, charge transfer boundary), the system exhibits insulating behavior. Positive V_{TG} (regime I) shows strong T -dependence, signaling enhanced electronic correlations, while negative V_{TG} (regime II) displays weak T -dependence. **b**, dR/dT map across V_{TG} and T . The curves are smoothed as detailed in the method section with $\Delta T = 2$ K and interpolated along V_{TG} at an interval of 0.15 V. The center insulating region corresponds to the charge transfer phase boundary, and the insulating region centered at $V_{\text{TG}} = 3$ V corresponds to another high-temperature insulating phase. Regime I and regime II align with Fig. 2a.

(< 10 K) insulating pocket forms. These phases collectively suggest competing electronic orders.

Strikingly, in-plane magnetic fields induce a metal-insulator transition in the middle band ($V_{\text{TG}} = 0.5$ V) while leaving the lower band ($V_{\text{TG}} = -1$ V) unaffected (Extended Data Figure S6), which is direct evidence of band-selective quantum phases. While mean-field theories capture Kondo coherence and the hybridization gap, the multiphase complexity, including competing insulating regimes and new incoherent Kondo scattering demands advanced frameworks incorporating magnetic frustration and lattice-mismatch effects. This system’s gate-tunable phase multiplicity establishes it as a unique platform for probing quantum criticality near competing orders.

Conclusion

The realization of heavy fermion behavior in the $\text{Nb}_3\text{Cl}_8/\text{MLG}$ heterostructure establishes a paradigm shift in correlated quantum material design. By coupling the Mott insulator and itinerant electron reservoir from distinct vdW layers, we bypass traditional lattice-matching constraints while retaining gate-controlled band structure, an achievement with profound implications for quantum engineering. The observed hybridization gap ($\Delta \approx 30$ meV) and order-of-magnitude electron effective mass dichotomy between regimes directly trace to interfacial Kondo screening, as captured by our SSMF framework. Crucially, the coexistence of hybridization gap, hidden-order, and critical metallic phases near charge transfer boundaries suggests proximity to a quantum critical point, where competing energy scales could host exotic non-Fermi liquid states. While residual discrepancies between theory and experiment hint at beyond-mean-

field effects, such as emergent spin textures or RKKY-mediated correlations²⁵, the system’s electrical tunability provides unprecedented access to these open questions.

This work transcends the specific $\text{Nb}_3\text{Cl}_8/\text{MLG}$ platform, offering a blueprint for quantum system synthesis via “Mott insulator + other material” strategy — from spin-orbit-coupled transition metal dichalcogenide (TMD)-based architectures²⁶ to non-zero Chern band-engineered (rhombohedral-stacked graphene)²⁷ heavy fermions. Such designer systems promise to unravel longstanding mysteries in quantum criticality while enabling novel device concepts, such as correlation-tunable superconducting qubits or frustration-driven topological insulators. The marriage of vdW assembly with heavy fermion physics thus marks a transformative frontier in both fundamental quantum matter research and post-Moore nanotechnology.

Methods

Crystal growth. Single crystals of Nb_3Cl_8 were grown using a PbCl_2 -flux method. Precursor Nb_3Cl_8 powder was first synthesized by solid-state reactions using high-purity Nb powder (Alfa Aesar, 99.99%) and NbCl_5 powder (Alfa Aesar, 99.9%) in a molar ratio of 7:8. The starting materials were thoroughly mixed, sealed in a quartz tube under vacuum, and heated at 700°C for 48 h. The obtained Nb_3Cl_8 precursor was then mixed with sufficient PbCl_2 flux, sealed, and vacuumed in the same way. The mixture was further heated to 750°C for 20 h, maintaining this temperature for 300 h. It was then slowly cooled to 500°C for 100 h, followed by natural cooling to room temperature. The Nb_3Cl_8 single crystals were finally obtained by removing the excessive flux using hot water.

Device fabrication. The few-layer Nb₃Cl₈ flake, monolayer graphene, and *h*-BN flake utilized in this study were subjected to mechanical exfoliation onto Si/SiO₂ substrates in ambient conditions. The Nb₃Cl₈/MLG heterostructures were meticulously assembled layer-by-layer using a poly (bisphenol A carbonate) film atop a poly-dimethylsiloxane (PDMS) stamp. The heterostructure was shaped into Hall-bar geometry and metallization through a series of steps involving electron-beam lithography, reactive ion etching, electron beam evaporation, and a lift-off process.

Transport measurements. Transport measurements were performed in a Heliox³ He insert system equipped with a 14 T superconducting magnet with the standard lock-in method. The low-frequency sine output of SR830 and a 1 MΩ resistance were used to provide a current excitation. Three SR830 lock-in amplifiers were used to measure the V_{xx} , V_{xy} , and the voltage on the 1 MΩ resistance. The 10 MΩ input impedance of SR830 is significantly larger than these resistances and thus will not affect the results. For temperature-dependent measurements, all data shown in the main text were collected while the sample was heated up. The heating rate was less than 2 K/min to ensure the sample temperature was identical with the thermometer. To circumvent the impact of the intricate phase at low temperatures, a top gate voltage sweep was conducted at 120 K, followed by cooling to the base temperature and subsequent heating back to 120 K to ascertain the *R-T* curve. The temperature-dependent Hall data was derived through anti-symmetrization the temperature-dependent R_{xy} at ± 4 kOe.

Data processing. The smooth and derivative calculation of *R-T* curves was performed simultaneously by applying a linear fit. For instance, to ascertain the *R* and dR/dT at temperature T_0 , the smooth range is defined as ΔT . All data points within the range of $|T - T_0| < \Delta T$ are extracted, and a linear fit is performed, denoted by $R = A(T - T_0) + B$. The intercept, *B*, corresponds to the smoothed resistance *R*, while the slope, *A*, represents the derivative dR/dT . The ΔT for Fig. 2c, Fig. 4a, and Extended data Figure S3 is 0.1 K, for Fig. 1e is 1 K, and for Fig. 4b is 2 K.

Density functional theory calculation. The first-principles calculation, based on DFT, was performed using Quantum ESPRESSO^{28,29}. The pseudopotentials C.pbe-n-kjpaw_psl.1.0.0.UPF, Nb.pbe-spn-kjpaw_psl.1.0.0.UPF, and Cl.pbe-n-kjpaw_psl.1.0.0.UPF are from the Quantum ESPRESSO pseudopotential database (<http://www.quantum-espresso.org/pseudopotentials>). The cutoff energy of the plane wave was set to 120 Ry. The calculation of the commensurate Nb₃Cl₈/MLG heterostructure utilized a monolayer Nb₃Cl₈ unit cell and a $\sqrt{7} \times \sqrt{7}$ supercell for monolayer graphene, with the distance between mirrors of the heterostructure exceeding 20 Å to avoid electron hopping between layers. The exchange-correlation potential employed was the generalized gradient approximation (GGA) by Perdew, Burke, and Ernzerhof. The magnetic state in the calculation was set to "non-polarized". The on-site Hubbard *U* of Nb was not included due to the fact that the band of interest is half-filled and sufficiently separated from other bands. Even with Hubbard *U*, the correct band structure (or spectral function) cannot be obtained with DFT. The crystal structure of the heterostructure underwent full relaxation, and the residual forces on the atoms did not exceed 0.03 eV/Å. The interlayer interaction was described using the "DFT-D2" van der Waals correction. A 30×30×1 k-space grid was employed in the self-consistent calculation.

Data Availability

The data that support the findings of this study will be available at an open-access repository with a doi link, when accepted for publishing.

Acknowledgements

This work was supported by the National Natural Science Foundation of China (No. 12425402 and No. 12250007) and the National Key R&D Program of China (No. 2022YFA1203902). K.W. and T.T. acknowledge support from the JSPSKAKENHI (No. 21H05233 and No. 23H02052) and World Premier International Research Center Initiative (WPI), MEXT, Japan.

Authors contributions

Y.Y. and Y.G. conceived the project. Y.G. fabricated the devices, performed the transport measurements, analyzed the data, and conducted the theoretical calculation with the help of W.Z., F. Y., X.H., and H.X.. Z.M. synthesized the Nb₃Cl₈ crystals under the supervision of Y.S.. K.W. and T.T. grew the *h*-BN bulk crystals. Y.G. and Y.Y. drafted the manuscript. All authors discussed the results and contributed to the manuscript.

Conflict of Interest

The authors declare no competing interests.

References

- [1] Stewart, G. Non-fermi-liquid behavior in d- and f-electron metals. *Reviews of modern Physics* **73**, 797 (2001).
- [2] Dzero, M., Xia, J., Galitski, V. & Coleman, P. Topological kondo insulators. *Annual Review of Condensed Matter Physics* **7**, 249–280 (2016).
- [3] Stockert, O. *et al.* Magnetically driven superconductivity in *cecu2si2*. *Nature Physics* **7**, 119–124 (2011).
- [4] Jiao, L. *et al.* Chiral superconductivity in heavy-fermion metal *ute2*. *Nature* **579**, 523–527 (2020).
- [5] Maksimovic, N. *et al.* Evidence for a delocalization quantum phase transition without symmetry breaking in *cecoin5*. *Science* **375**, 76–81 (2022).
- [6] Paschen, S. *et al.* Hall-effect evolution across a heavy-fermion quantum critical point. *Nature* **432**, 881–885 (2004).
- [7] Zhao, W. *et al.* Gate-tunable heavy fermions in a moiré kondo lattice. *Nature* **616**, 61–65 (2023).
- [8] Vaño, V. *et al.* Artificial heavy fermions in a van der waals heterostructure. *Nature* **599**, 582–586 (2021).
- [9] Gao, S. *et al.* Discovery of a single-band mott insulator in a van der waals flat-band compound. *Phys. Rev. X* **13**, 041049 (2023). URL <https://link.aps.org/doi/10.1103/PhysRevX.13.041049>.
- [10] Grytsiuk, S., Katsnelson, M. I., Loon, E. G. v. & Rösner, M. Nb₃cl₈: a prototypical layered mott-hubbard insulator. *npj Quantum Materials* **9**, 8 (2024).

- [11] Liang, Y. *et al.* A universal model for accurately predicting the formation energy of inorganic compounds. *Science China Materials* **66**, 343–351 (2022).
- [12] Kadowaki, K. & Woods, S. Universal relationship of the resistivity and specific heat in heavy-fermion compounds. *Solid state communications* **58**, 507–509 (1986).
- [13] Wang, Y. *et al.* Quantum hall phase in graphene engineered by interfacial charge coupling. *Nature Nanotechnology* **17**, 1272–1279 (2022).
- [14] Yang, K. *et al.* Unconventional correlated insulator in crocl-interfaced bernal bilayer graphene. *Nature Communications* **14**, 2136 (2023).
- [15] Chen, L. *et al.* Emergent flat band and topological kondo semimetal driven by orbital-selective correlations. *Nature Communications* **15**, 5242 (2024).
- [16] De Leo, L., Civelli, M. & Kotliar, G. T= 0 heavy-fermion quantum critical point as an orbital-selective mott transition. *Physical review letters* **101**, 256404 (2008).
- [17] Pépin, C. Kondo breakdown as a selective mott transition in the anderson lattice. *Physical review letters* **98**, 206401 (2007).
- [18] Schäfer, T., Katanin, A., Kitatani, M., Toschi, A. & Held, K. Quantum criticality in the two-dimensional periodic anderson model. *Physical Review Letters* **122**, 227201 (2019).
- [19] Riseborough, P. S. Collapse of the coherence gap in kondo semiconductors. *Physical Review B* **68**, 235213 (2003).
- [20] Pietrus, T., v. Löhneysen, H. & Schlottmann, P. Kondo-hole conduction in the la-doped kondo insulator ce 3 bi 4 pt 3. *Physical Review B—Condensed Matter and Materials Physics* **77**, 115134 (2008).
- [21] Varma, C. Mixed-valence compounds. *Reviews of Modern physics* **48**, 219 (1976).
- [22] Guan, Z., Ni, S. & Hu, S. Band gap opening of graphene by forming a graphene/ptse 2 van der waals heterojunction. *RSC advances* **7**, 45393–45399 (2017).
- [23] Das, D. *et al.* Magnetic field driven complex phase diagram of antiferromagnetic heavy-fermion superconductor ce3ptin11. *Scientific Reports* **8**, 16703 (2018).
- [24] Wang, L. *et al.* Heavy fermion behavior in the quasi-one-dimensional kondo lattice ceco2ga8. *npj Quantum Materials* **2**, 36 (2017).
- [25] Gleis, A., Lee, S.-S. B., Kotliar, G. & Von Delft, J. Emergent properties of the periodic anderson model: A high-resolution, real-frequency study of heavy-fermion quantum criticality. *Physical Review X* **14**, 041036 (2024).
- [26] Yang, B. *et al.* Strong electron-hole symmetric rashba spin-orbit coupling in graphene/monolayer transition metal dichalcogenide heterostructures. *Physical Review B* **96**, 041409 (2017).
- [27] Han, T. *et al.* Correlated insulator and chern insulators in pentalayer rhombohedral-stacked graphene. *Nature Nanotechnology* **19**, 181–187 (2024).
- [28] Giannozzi, P. *et al.* Quantum espresso: a modular and open-source software project for quantum simulations of materials. *Journal of Physics: Condensed Matter* **21**, 395502 (19pp) (2009). URL <http://www.quantum-espresso.org>.
- [29] Giannozzi, P. *et al.* Advanced capabilities for materials modelling with quantum espresso. *Journal of Physics: Condensed Matter* **29**, 465901 (2017). URL <http://stacks.iop.org/0953-8984/29/i=46/a=465901>.